EDGE ARTICLE

Check for updates

Crystal clear: unveiling giant birefringence in organic–inorganic cocrystals†

Yang Li [ID] and Kang Min Ok [ID] *

Coplanar groups with large anisotropic polarizability are suitable as birefringence-active groups for investigating compounds with significant birefringence. In this study, the organic coplanar raw reagent, o-C_5H_5NO (**4HP**), was selected as an individual complement. Utilizing the cocrystal engineering strategy, we successfully designed two cocrystals: $[LiNO_3 \cdot H_2O \cdot \textbf{4HP}] \cdot \textbf{4HP}$ (**Li-4HP2**) and $[Mg(NO_3)_2 \cdot 6H_2O] \cdot (\textbf{4HP})_2$ (**Mg-4HP**), and one by-product: $LiNO_3 \cdot H_2O \cdot \textbf{4HP}$ (**Li-4HP**), which were grown using a mild aqua-solution method. The synergy of the coplanar groups of NO_3^- and **4HP** in the structures resulted in unexpectedly large birefringence values of 0.376–0.522@546 nm. Furthermore, the compounds exhibit large bandgaps (4.08–4.51 eV), short UV cutoff edges (275–278 nm), and favorable growth habits, suggesting their potential as short-wave UV birefringent materials.

Introduction

Cocrystals are an important class of compounds with unique properties, widely utilized in ferroelectricity, ambipolar charge transport, photovoltaics, *etc.*[1–5] In general, noncovalent inter-actions assemble neutral molecules in a stoichiometric ratio to construct the cocrystal, which is beneficial for synthesizing the cocrystal under mild conditions. In addition, the facile selection of components could effectively design and tune the structure and properties of the target cocrystal.[6–8] Therefore, the cocrystal engineering strategy has been proposed and widely applied to investigate and grow large sized new nonlinear optical/birefringent materials, including compounds in the $AX \cdot H_3C_3$-N_3O_3 family,[9–11] $KF \cdot B(OH)_3$,[12] $RbCl \cdot H_2SeO_3$,[13] $(NH_4HCOO)_3[$-$B(OH)_3]_2$,[14] $KNO_3 \cdot NH_3SO_3$,[15] $KIO_3 \cdot Te(OH)_6$,[16] $K_2SO_4 \cdot (SbF_3)_2$,[17] and $K_2SO_4 \cdot HIO_3$.[18]

Birefringent crystals can modulate and control light polarization, making them extensively utilized in laser-related fields.[19–23] Commercial birefringent materials, such as MgF_2, α-BaB_2O_4 (α-BBO), $CaCO_3$, TiO_2, and $LiNbO_3$, play critical roles across the deep ultraviolet (DUV) to near-infrared (NIR) regions.[24–28] However, distinct limitations, such as the phase transition in α-BBO and the difficulty in growing high-quality $CaCO_3$ crystals, make exploring new birefringent materials with substantial birefringence in the short-wave UV region an urgent and significant endeavor.

Birefringence-active groups with large anisotropic polarizability ($\Delta\alpha$) are the cornerstone for designing birefringent materials.[29] π-Conjugated groups with delocalized electrons and cations with lone pair electrons exhibit large $\Delta\alpha$, making them suitable birefringence-active groups.[30–34] In contrast, the nearly isotropic distribution of electronic clouds in halogens results in rigid regular tetrahedral groups such as TO_4 (T = B, Si, P, S, *etc.*) having $\Delta\alpha$ close to zero.[35] Hence, π-conjugated systems such as MO_3 (M = B, C, and N) groups, and benzene-like six-membered ring groups (B_3O_6) are among the hotspots for investigating birefringent materials.[36–40] Consequently, classical birefringent materials including α-BBO,[25] $CaCO_3$,[26] and $NaNO_3$ have been investigated.[41] Among the MO_3 (M = B, C, and N) family, NO_3 exhibits the shortest bond length, indicating a more substantial overlap between N 2p and O 2p orbitals. This overlap results in heightened p_π–p_π interactions, yielding the largest $\Delta\alpha$ within the MO_3 family.[42] Besides, B_3O_6, composed of three BO_3 units, attains a '1 + 1 + 1 > 3' configuration, affirming the suitability of six-membered rings as birefringence-active groups.[42]

Recent research has expanded exploration from the traditional inorganic π-conjugated system to the organic system.[43] Organic six-membered ring groups (6-MRs) have been identified as excellent birefringence-active groups with considerably larger $\Delta\alpha$, such as $[H_xC_3N_3O_3]^{(3-x)-}$ ($x = 0$–3) and $C_3N_6H_7^+$.[44–47] As a result, organic 6-MR compounds with substantial birefringence have been reported.[48–50]

However, although NO_3^- and organic 6-MRs have attractive $\Delta\alpha$, these groups will red-shift the bandgaps, posing an obstacle to their potential application in the UV region. Therefore, it is still necessary to introduce alkali and alkaline earth metal cations without *d–d/f–f* electron transitions to enlarge the bandgap.

Department of Chemistry, Sogang University, Seoul 04107, Republic of Korea. E-mail: kmok@sogang.ac.kr

Strong covalent cations including Li^+ and Mg^{2+} draw our attention due to the benefits of enlarging bandgaps. Besides, they can easily form hydrate cations in the water solution system: for example, Mg^{2+} tends to form the hydrated $[Mg(H_2O)_6]^{2+}$, which could serve as a good hydrogen bonding donor to govern the distribution of NO_3^- and oxygen heterocycle groups and construct the cocrystal.

Inspired by the above ideas, we decided to explore the Li/Mg-NO_3-4HP system for hybrid organic–inorganic cocrystals with giant birefringence. Using the cocrystal approach, $LiNO_3 \cdot H_2O \cdot 4HP$ (Li-4HP), $[LiNO_3 \cdot H_2O \cdot 4HP] \cdot 4HP$ (Li-4HP2), and $[Mg(NO_3)_2 \cdot 6H_2O] \cdot (4HP)_2$ (Mg-4HP) were grown via the mild slow evaporation method. They exhibit short UV cutoff edges (275–278 nm) and giant birefringence (0.376–0.522@546 nm), thus being promising short-wave UV birefringent crystals. Li-4HP2 demonstrates a giant birefringence of 0.522@546 nm, which is the largest among those reported for inorganic–organic hybrid cocrystals in the short-wave UV region. This study serves an exemplary illustration of successful exploration into novel short-wave UV birefringent crystals with giant birefringence and wide bandgaps using the cocrystal approach.

Experimental section

Single crystals of compounds Li-4HP, Li-4HP2, and Mg-4HP were grown via the aqua-solution method at room temperature. $LiNO_3$ (Sigma, 10 mmol) and 4HP (TCI, >99%, 10 mmol) were used for Li-4HP, with the 4HP amount increased to 20 mmol for Li-4HP2. A mixture of $Mg(NO_3)_2 \cdot 6H_2O$ (DAE-JUNG, 98%, 10 mmol) and 4HP (20 mmol) was used for Mg-4HP. After one week, colorless bulk crystals of Li-4HP2 and Mg-4HP (with sizes up to $2 \times 1 \times 0.5$ cm^3) and millimeter-level needle-like crystals of Li-4HP were obtained. These crystals were washed with distilled water for subsequent measurements. The polycrystalline samples were prepared by directly grinding the as-grown crystals and checked using powder X-ray diffraction.

The powder X-ray diffraction data were collected via the Mini Flex 600 diffractometer using Cu Kα ($\lambda = 1.54406$ Å) radiation with 40 kV and 15 mA at room temperature. The sample was scanned in the 2θ range of 5–70° at a scan speed of 10° min^{-1} and a scan step width of 0.02°. The measured diffraction pattern of the title compounds matched well with the simulated one (Fig. S1 and S4†).

The crystal structures were determined via a Bruker D8 QUEST diffractometer with a Mo Kα radiation source ($\lambda = 0.71073$ Å) at the Advanced Bio-Interface Core Research Facility at Sogang University at room temperature. The SAINT and SADABS programs were used for data reduction and absorption correction, respectively.[51] The OLEX2 package was used to solve and refine the structure.[52] Solved structures were checked using PLATON to avoid any missing higher symmetry.[53] Crystallographic data, structure refinement information, atomic coordinates, equivalent isotropic displacement parameters, selected bond lengths, and bond angle are listed in the ESI (Tables S1–S5).†

Infrared (IR) spectra were recorded using a Thermo Scientific Nicolet iS50 FT-IR spectrometer. The ground sample was placed on the diamond attenuated total reflectance crystal (Fig. S2†).

The ultraviolet-visible-near infrared (UV-vis-NIR) transmittance spectrum for Mg-4HP was obtained using a Shimadzu SolidSpec-3700 DUV spectrophotometer at room temperature in the 200–1600 nm wavelength range. The UV-vis diffuse-reflectance spectra for Li-4HP, Li-4HP2 and Mg-4HP, and 4HP were recorded on a Lambda 1050 scan UV-vis spectrophotometer at room temperature, covering the spectral range of 200–800 nm.

Thermogravimetric analysis (TGA) was conducted using a SCINCO TGA-N 1000 thermal analyzer. The ground polycrystalline samples were loaded into alumina crucibles and heated to 900 °C at a rate of 10 °C min^{-1} under flowing air (Fig. S3†).

Single crystals of Li-4HP2 (0.0469 g) and Mg-4HP (1.1771 g), and a polycrystalline sample of Li-4HP (0.6125 g) were used to quantify the change in weight after exposure to air over seven days. The ambient temperature and humidity were maintained at 25 ± 5 °C and $36 \pm 5\%$, respectively.

The polarizability anisotropy for NO_3^- and 4HP was calculated using Gaussian 09 at the B3LYP/6-31G level and analyzed by Multiwfn.[54,55] CP2K (version 2022.1) was applied to calculate the electron localization function (ELF) at the B3LYP/6-311G* level (Fig. S5†).[56] The CASTEP package (version 23.1) was utilized for the first-principles calculations based on density-functional theory.[57] Band structure, density of states, and optical properties were calculated using the Perdew–Burke–Ernzerhof (PBE) generalized gradient approximation (GGA) and the norm-conserving pseudopotential (NCP).[58–61] The valence electrons (cutoff energy) of the pseudo-potential used are as follows: H $1s^1$ (650 eV), C $2s^2 2p^2$ (680 eV), N $2s^2 2p^3$ (700 eV), O $2s^2 2p^4$ (750 eV), Li $2s^1$ (450 eV), and Mg $2s^2 2p^6 3s^2$ (900 eV). A plane-wave cut-off energy of 990 eV for Mg-4HP and $Mg(NO_3)_2 \cdot 6H_2O$, and 830 eV for Li-4HP and Li-4HP2 were chosen. A dense k-point sampling of less than 0.04 Å^{-1} was adopted for geometry optimization and calculation of optical properties (Fig. S6–S7†). Other parameters were set at the ultrafine level as default.

Results and discussion

Li-4HP crystallizes in the monoclinic space group, $P2_1/n$ (no. 14) with unit cell parameters of $a = 8.821(8)$ Å, $b = 10.477(9)$ Å, $c = 9.205(9)$ Å, $\beta = 110.89(3)°$, and $V = 794.8$ Å^3. Li^+ is five-coordinated with oxygen atoms and generated the $[LiO_4H_2O]^{7-}$ polyhedra. The $[LiO_4H_2O]^{7-}$ polyhedra are corner-sharing the O1 atom with 4HP, edge-sharing the O3 and O4 atoms with NO_3, and edge-sharing the O1–O1 with the adjacent $[LiO_4H_2O]^{7-}$ polyhedra to form the $[LiNO_3 \cdot H_2O \cdot 4HP]_2$ dimer (Fig. 1a). In the dimer, the distances between Li and O, and between N and O, are in the ranges of 1.940 to 2.552 Å and 1.244 to 1.252 Å, respectively. The dihedral angle between 4HP and NO_3^- is 85.06° (Fig. S8†). This nearly vertical arrangement benefits the dimer further by connecting adjacent $[LiNO_3 \cdot H_2O \cdot 4HP]_2$ dimers through hydrogen bonds of O/N–H⋯O, generating pseudo-layers of $\{[LiNO_3 \cdot H_2O \cdot 4HP]_2\}^0$ in the ac plane (Fig. 1b). The dihedral angle between adjacent pseudo-layers (A and B) is 87.88°. These pseudo-layers further stack
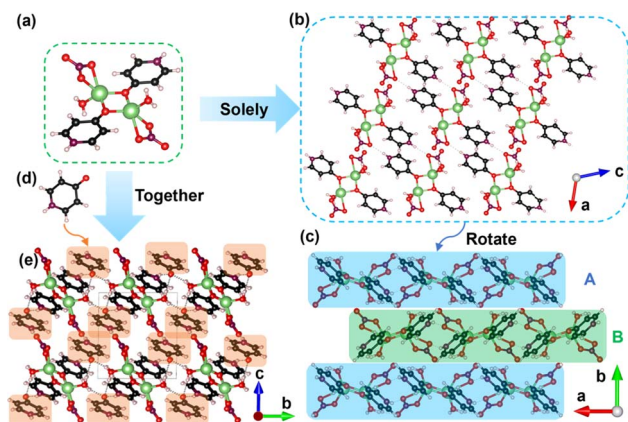
Fig. 1 Ball-and-stick representations of (a) the $[\text{LiNO}_3 \cdot \text{H}_2\text{O} \cdot \textbf{4HP}]_2$ dimer and pseudo-layers of $\{[\text{LiNO}_3 \cdot \text{H}_2\text{O} \cdot \textbf{4HP}]_2\}^0$ viewed along (b) the *b*-axis and (c) *c*-axis for **Li-4HP**. (d and e) The additional neutral **4HP** separates the $[\text{LiNO}_3 \cdot \text{H}_2\text{O} \cdot \textbf{4HP}]_2$ dimers and generates a pseudo-three-dimensional structure of **Li-4HP2** (black, C; purple, N; red, O; white, H; green, Li).
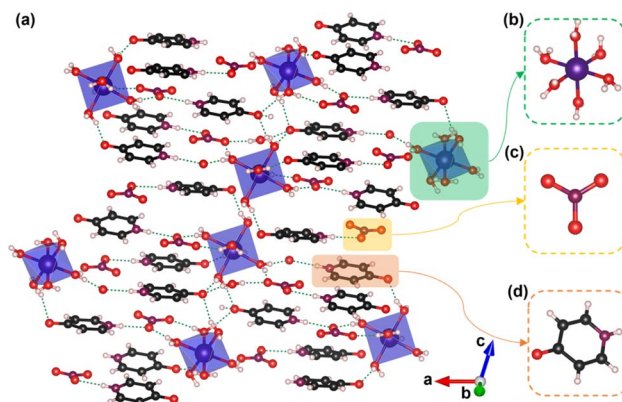

Fig. 2 Ball-and-stick and polyhedral representations of (a) Mg-4HP viewed along the *b*-axis (black, C; purple, N; red, O; blue, Mg; white, H). (b) $[\text{Mg}(\text{H}_2\text{O})_6]^{2+}$, (c) NO_3^-, and (d) **4HP** groups are highlighted.

along the *b*-axis with an ABAB arrangement, generating the final pseudo-two-dimensional structure (Fig. 1c).

Li-4HP2 crystallizes in the triclinic space group, $P\bar{1}$ (no. 2) with unit cell parameters of $a = 8.2120(6)$ Å, $b = 8.9624(6)$ Å, $c = 9.9320(7)$ Å, $\alpha = 82.101(2)°$, $\beta = 106.673(2)°$, $\gamma = 70.184(2)°$, and $V = 638.59$ Å^3. As depicted in the formula, it is composed of the $[\text{LiNO}_3 \cdot \text{H}_2\text{O} \cdot \textbf{4HP}]_2$ dimer and one additional **4HP** (Fig. 1a and d). With the additional 4HP introduced into the lattice, the dihedral angle between **4HP** and NO_3^- in the $[\text{LiNO}_3 \cdot \text{H}_2\text{O} \cdot \textbf{4HP}]_2$ dimer was decreased from 85.06° to 32.03° (Fig. S8†). Among the $[\text{LiNO}_3 \cdot \text{H}_2\text{O} \cdot \textbf{4HP}]_2$ dimer, the bond lengths of Li–O range from 1.935 to 2.333 Å, and the distances between N and O atoms range from 1.246 to 1.252 Å. It should be noticed that in **Li-4HP2**, adjacent $[\text{LiNO}_3 \cdot \text{H}_2\text{O} \cdot \textbf{4HP}]_2$ dimers are assembled, generating the pseudo-layers of $\{[\text{LiNO}_3 \cdot \text{H}_2\text{O} \cdot \textbf{4HP}]_2\}^0$. However, in **Li-4HP2**, the additional neutral **4HP** separates these $[\text{LiNO}_3 \cdot \text{H}_2\text{O} \cdot \textbf{4HP}]_2$ dimers and generates the final pseudo-three-dimensional structure (Fig. 1e). Interestingly, the **4HP** is nearly parallel to the distribution of the structure, indicating that the individual **4HP** plays a key role in governing the arrangements of coplanar groups in **Li-4HP2**.

Mg-4HP crystallizes in the monoclinic space group, $I2/a$ (no. 15) with unit cell parameters of $a = 24.6517(11)$ Å, $b = 6.4107(3)$ Å, $c = 26.2782(12)$ Å, $\beta = 106.673(2)°$, and $V = 3978.27$ Å^3. An asymmetric unit consists of one $[\text{Mg}(\text{H}_2\text{O})_6]^{2+}$ octahedron, two NO_3^- groups, and **4HP** groups, which agrees with the chemical formula (Fig. 2b–d). The Mg–O distances range from 2.032 to 2.080 Å, and the corresponding distortion (Δd) is 0.089. Thus, weak distortion makes little contribution to the birefringence. The distances between N and O atoms in the NO_3^- groups range from 1.221 to 1.259 Å. The bond lengths of C–O and C–N fall into the range of 1.278 to 1.282 Å and 1.333 to 1.345 Å, respectively, matching well with reported compounds. Hydrogen bonds of O–H⋯O were observed among the $[\text{Mg}(\text{H}_2\text{O})_6]^{2+}$ octahedron, coplanar NO_3^- and **4HP** groups. Hydrogen bonding interactions between N2–H2 in **4HP** and

O13–N3 from NO_3^- were observed, generating the $[(\text{NO}_3) \cdot (\textbf{4HP})]^-$ dimer. The NO_3^- and **4HP** are nearly parallel in the dimer, and the dihedral angles range from 1.45 to 14.88° (Fig. S9†). The hydrogen bonds further assemble this dimer and the $[\text{Mg}(\text{H}_2\text{O})_6]^{2+}$ octahedron, constructing the final pseudo-three-dimensional structure (Fig. 2a).

The IR spectra in Fig. S2† reveal the characteristic vibrations of **4HP** ($v_{\text{C=O}}$ at 1645 cm^{-1}, $v_{\text{N–H}}$ at 3230 cm^{-1}), MgO_6 ($v_{\text{Mg–O}}$ at 824 and 1402 cm^{-1}), H_2O (peak at 3411 cm^{-1}), and NO_3 (peaks at 850, 769 and 715 cm^{-1}), respectively.[62–64]

UV-vis diffuse reflectance spectra suggest that the compounds **Li-4HP**, **Li-4HP2**, **Mg-4HP**, and **4HP** possess short UV cutoff edges of 276, 278, 275, and 291 nm, respectively (Fig. 3). A polished crystal of compound **Mg-4HP** with a suitable size was selected to measure the UV-vis-NIR transmittance spectrum (Fig. S10†). At 275 nm, the transmittance remains at 0.02%, which corresponds well to the diffuse reflectance result. The corresponding bandgaps are 4.08, 4.15, 4.51, and 3.95 eV for compounds **Li-4HP**, **Li-4HP2**, **Mg-4HP**, and **4HP**, respectively
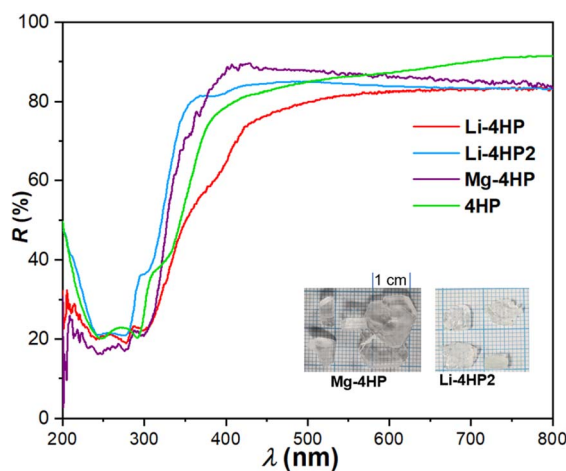

Fig. 3 UV-vis diffuse reflectance spectra for **Li-4HP**, **Li-4HP2**, **Mg-4HP** and **4HP**. (Inset): As-grown crystals of **Mg-4HP** (left) and **Li-4HP2** (right).

(Fig. S11†). Therefore, these three compounds, with broad bandgaps, could potentially be birefringent crystals applicable in the short-wave UV region.

The thermal stability data indicate that during the heating of **Li-4HP**, **Li-4HP2**, and **Mg-4HP** from 25 to 900 °C, they lose water molecules in the first step (for **Li-4HP**, cal. 9.9%, exp. 9.9%; for **Li-4HP2**, cal. 6.5%, exp. 6.5%; for **Mg-4HP**, cal. 24.2%, exp, 22.8%). The subsequent step for **Li-4HP** and **Li-4HP2** involves the loss of CO_2, H_2O, and N_2, forming Li_2CO_3. The subsequent step involves the loss of the organic molecule **4HP** and nitrate, finally generating the corresponding oxides, Li_2O (for **Li-4HP**, cal. 8.2%, exp. 6.8%; for **Li-4HP2**, cal. 6.2%, exp. 7.4%) and MgO (for **Mg-4HP**, cal. 9.2%, exp. 11.7%) (Fig. S3†).

After exposure to air for seven days, **Li-4HP**, **Li-4HP2**, and **Mg-4HP** exhibited almost no change in mass. In addition, PXRD patterns measured after exposure to air for a week confirm that all the reported samples have good air stability under ambient temperature and humidity conditions (Fig. S4†). The band structures indicate that **Li-4HP**, **Li-4HP2**, and **Mg-4HP** belong to the class of direct bandgap compounds. The calculated bandgaps are 3.41, 3.47, and 3.11 eV, respectively, which are smaller than the experimental bandgaps (Fig. S6†). The differences were applied as scissor corrections to analyze the optical properties. In all three compounds, the upper regions of the valence band (VB) are mainly occupied by the C/N/O 2p states, with a small contribution from the H 1s states. The bottom of the conduction band (CB) consists of C/N/O 2p and Li 2p states (**Li-4HP** and **Li-4HP2**), respectively. These results suggest that the organic group of **4HP** primarily determines the optical properties of these compounds (Fig. S7†). As revealed by the electron localization function (ELF) diagrams in Fig. S5,† delocalized π bonds were observed in the NO_3^- and **4HP** of both **Li-4HP**, **Li-4HP2**, and **Mg-4HP**. The synergistic effect of NO_3^- and **4HP** endows these compounds with giant optical anisotropy, as expected.

The relationship between wavelength and the birefringence is depicted in Fig. S12 and S13.† The calculated birefringence values for **Li-4HP**, **Li-4HP2**, and **Mg-4HP** are 0.387, 0.546, and 0.376 (0.227 on the (100) plane), respectively. Crystals of **Li-4HP**, **Li-4HP2**, and **Mg-4HP** (on the (100) plane) were measured using a cross-polarizing microscope. The optical path differences (R) at 546 nm are 3.620, 8.265, 1.799 μm, with thicknesses of 10, 15.823, and 7.951 μm (Fig. 5, S14 and S15†). Derived from the formula: $R = d \times \Delta n$, the birefringence at 546 nm is calculated as 0.362, 0.522, and 0.226, closely matching the calculated values of 0.387, 0.546, and 0.227. The measured birefringence of **Mg-4HP** is limited because the only natural crystal plane suitable for measurement is the (100) crystal plane, and thus it does not reach the largest birefringence of 0.376@546 nm. However, the measured value of 0.226@546 nm still fits the calculated birefringence on the (100) crystal plane well. Such giant birefringence is significantly larger than those of commercial birefringent materials such as α-BaB_2O_4 (0.122 @532 nm) and YVO_4 (0.225 @633 nm) (Fig. 4).[25,65] Besides, **Li-4HP2** exceeds other reported organic–inorganic hybrid cocrystals in the short-wave UV region. For example, $ANO_3 \cdot H_3C_3N_3O_3$ (A = K and Rb) has values ranging from 0.243 to 0.268 @546.1 nm,[66] $AX \cdot (H_3C_3N_3-O_3)_x$ (A = alkali metal cations, X = Cl/Br/I, x = 1–2) ranges from
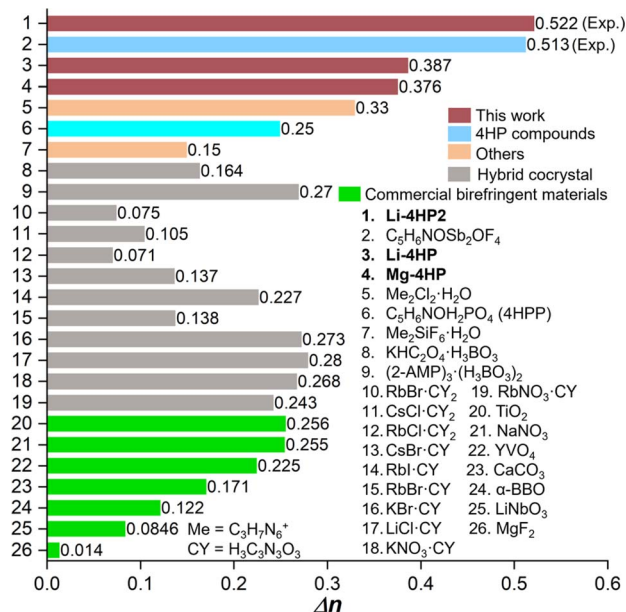

Fig. 4 Calculated (experimental) birefringence values for Li-4HP, Li-4HP2, and Mg-4HP (@546 nm) compared with reported values for other birefringent crystals.
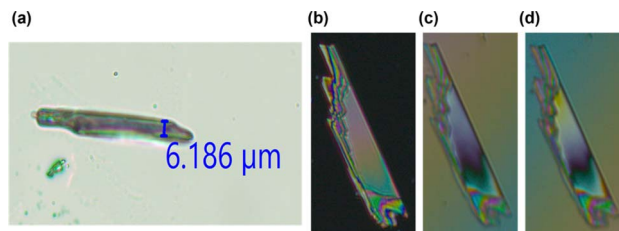

Fig. 5 (a) Thickness of a Li-4HP2 crystal and (b–d) a Li-4HP2 crystal observed under cross-polarized light, achieving complete extinction under a polarizing microscope.

0.071 to 0.28 @800 nm,[9,11,67,68] and $KHC_2O_4 \cdot (H_3BO_3)$ has a value of 0.164@1064 nm.[69] **Li-4HP2** also surpasses most 6-MR compounds, including **4HPP** (0.25@1064 nm),[48] β-$(C_3N_6H_7)_2$-$Cl_2 \cdot H_2O$ (0.38@550 nm),[70] $(C_3N_6H_7)_2SiF_6 \cdot H_2O$ (0.152@550 nm), and recently reported $C_5H_6NOSb_2OF_4$ (0.513@546 nm).[71,72]

To gain a deeper understanding of the origin of the giant optical anisotropy in **Mg-4HP**, the raw reagent $Mg(NO_3)_2 \cdot 6H_2O$ (ICSD 80446) was selected as a reference. In the structures of $Mg(NO_3)_2 \cdot 6H_2O$ and **Mg-4HP**, both coplanar groups (NO_3^- and **4HP**) are nearly ideally distributed, but with different spatial densities in the lattice (Fig. S18 and S19†). According to DFT calculations, the predicted birefringence of $Mg(NO_3)_2 \cdot 6H_2O$ is 0.198@546 nm, while **Mg-4HP** exhibits a larger birefringence of 0.376@546 nm, despite the spatial density of NO_3^- (4.02×10^{-3} Å^{-3}) being nearly half that in **Mg-4HP** (7.82×10^{-3} Å^{-3}). This indicates that the **4HP** group primarily contributes to the larger birefringence observed in **Mg-4HP**.

Herein, we establish a model to illustrate the contribution to birefringence from each coplanar group more intuitively. It is well known that the birefringence is related to the density,

polarizability, and spatial arrangement of the birefringence-active groups. In other words, Δn is proportional to $\rho \times \Delta\alpha \times \cos\theta$, where θ is the dihedral angle between the birefringence-active groups. To simplify this model, we assume that the large birefringence is solely attributed to the coplanar groups of NO_3^- and **4HP**, and the contribution from $[Mg(H_2O)_6]^{2+}$ and $[LiO_4H_2O]^{7-}$ polyhedra is almost negligible due to their small $\Delta\alpha$. In $Mg(NO_3)_2 \cdot 6H_2O$, NO_3^- is the sole birefringence-active group with a nearly parallel arrangement in the lattice. Therefore, it can be used as a benchmark to estimate the contribution to birefringence from the NO_3^- and **4HP** groups in **Mg-4HP**. A rough calculation of the contribution to birefringence (@546 nm) from NO_3^- in **Mg-4HP** is approximately $0.198/7.82 \times 4.02 = 0.102$, indicating that **4HP** contributes the remaining 0.274. Interestingly, in **Mg-4HP**, the ratio of Δn (**4HP**) to Δn (NO_3^-) is 2.69, which aligns well with the polarizability results of $\Delta\alpha$ (**4HP**) to $\Delta\alpha$ (NO_3^-) = 2.72. This observation highlights the synergistic effect of **4HP** and NO_3^- in endowing the large birefringence of **Mg-4HP**. Guided by this idea, the deduced contribution to birefringence (@546 nm) from **4HP** and NO_3^- is 0.427 and 0.060, and thus the deduced birefringence is 0.487, also very close to the measured value of 0.522 (Fig. 6). The slightly larger margin of error for **Li-4HP2** should be related to underestimating the distorted $\Delta\alpha$ (NO_3^-) and not taking the contribution from the distorted $[LiO_4H_2O]^{7-}$ polyhedra into account. However, this simplified model can still be used to reveal the contribution to birefringence from each coplanar group.

The above model indicates that the giant birefringence of **Li-4HP2** derives from the synergetic effect of the high spatial

density of **4HP** and NO_3^- groups. Interestingly, both **Li-4HP2** and **Mg-4HP** are **4HP**-NO_3^--based cocrystals, with **4HP** primarily affecting the birefringence. However, the spatial density of **4HP** is increased by nearly 35.8% (from 4.02 in **Mg-4HP** to 6.26×10^{-3} Å^{-3} in **Li-4HP2**), attributed to the following two reasons: First, in the solution system, Mg^{2+} tends to form the isolated $[Mg(H_2O)_6]^{2+}$ octahedra, where the six water molecules dilute the spatial density of **4HP** in the structure. Second, $[Mg(H_2O)_6]^{2+}$ octahedra can only weakly connect surrounding **4HP** and NO_3^- groups *via* hydrogen bonds, further diluting the spatial density of **4HP**. In contrast, in **Li-4HP2**, Li^+ connects the **4HP** and NO_3^- *via* stronger covalent Li–O bonds, resulting in a tighter interaction. In addition, the edge-sharing connection in the $[LiNO_3 \cdot H_2O \cdot 4HP]_2$ dimer further increases the spatial density of **4HP** in **Li-4HP2**.

Conclusions

In conclusion, we successfully synthesized two inorganic–organic hybrid cocrystals, **Li-4HP2**, and **Mg-4HP**, alongside a by-product, **Li-4HP**, utilizing a mild aqueous method, resulting in the growth of large crystals. These compounds exhibit substantial bandgaps ranging from 4.08 to 4.51 eV and demonstrate short UV cutoff edges between 275 and 278 nm. The nearly parallel distribution and higher spatial density of coplanar groups contribute to **Li-4HP2** displaying a remarkable birefringence of 0.522@546 nm. Our first-principles calculations reveal that the organic **4HP**, with its large polarizability, significantly enhances the birefringence observed. Coupled with their ease of growth, short UV cutoff edges, large bandgaps, and impressive birefringence, these compounds emerge as promising candidates for short-wave UV birefringent materials. This study serves as a successful illustration of exploring novel birefringent materials with enhanced birefringence within the cocrystal system.

Data availability

The data that support this article are available within the article and its ESI.†

Author contributions

KMO and YL conceived and designed the project and wrote the manuscript. YL carried out materials synthesis and characterization, as well as performed data analysis. KMO contributed to project administration and funding acquisition. All authors discussed the results and commented on the manuscript.

Conflicts of interest

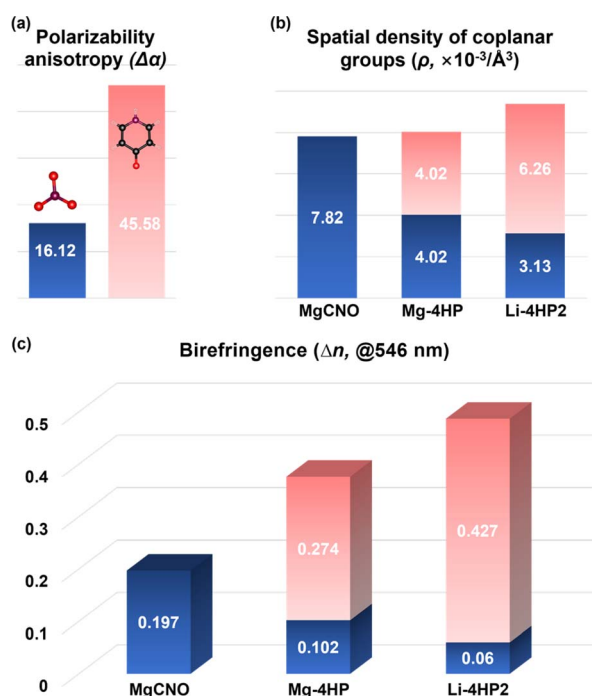There are no conflicts to declare.

Acknowledgements

Fig. 6 (a) Polarizability anisotropy ($\Delta\alpha$) of NO_3^- and **4HP**. (b) Spatial density (ρ) of coplanar birefringence-active functional building blocks (FBBs) in each compound (blue, NO_3^-; red, **4HP**, MgNO is $Mg(NO_3)_2 \cdot 6H_2O$). (c) Calculated and deduced birefringence (@546 nm) from each coplanar birefringence-active FBB.

Notes and references

1 L. Sun, W. Zhu, X. Zhang, L. Li, H. Dong and W. Hu, *J. Am. Chem. Soc.*, 2021, **143**, 19243–19256.

2 S. Aitipamula, R. Banerjee, A. K. Bansal, K. Biradha, M. L. Cheney, A. R. Choudhury, G. R. Desiraju, A. G. Dikundwar, R. Dubey, N. Duggirala, P. P. Ghogale, S. Ghosh, P. K. Goswami, N. R. Goud, R. R. K. R. Jetti, P. Karpinski, P. Kaushik, D. Kumar, V. Kumar, B. Moulton, A. Mukherjee, G. Mukherjee, A. S. Myerson, V. Puri, A. Ramanan, T. Rajamannar, C. M. Reddy, N. Rodriguez-Hornedo, R. D. Rogers, T. N. G. Row, P. Sanphui, N. Shan, G. Shete, A. Singh, C. C. Sun, J. A. Swift, R. Thaimattam, T. S. Thakur, R. Kumar Thaper, S. P. Thomas, S. Tothadi, V. R. Vangala, N. Variankaval, P. Vishweshwar, D. R. Weyna and M. J. Zaworotko, *Cryst. Growth Des.*, 2012, **12**, 2147–2152.

3 G. R. Desiraju, *CrystEngComm*, 2003, **5**, 466–467.

4 D. Yan and D. G. Evans, *Mater. Horiz.*, 2014, **1**, 46–57.

5 S. Horiuchi, F. Ishii, R. Kumai, Y. Okimoto, H. Tachibana, N. Nagaosa and Y. Tokura, *Nat. Mater.*, 2005, **4**, 163–166.

6 L. Sun, Y. Wang, F. Yang, X. Zhang and W. Hu, *Adv. Mater.*, 2019, **31**, 1–22.

7 G. Bolla, B. Sarma and A. K. Nangia, *Chem. Rev.*, 2022, **122**, 11514–11603.

8 Y. Wang, W. Zhu, W. Du, X. Liu, X. Zhang, H. Dong and W. Hu, *Angew. Chem., Int. Ed.*, 2018, **57**, 3963–3967.

9 X. Meng, K. Kang, Y. Liu, J. Tang, X. Jiang, W. Yin, Z. Lin and M. Xia, *Cryst. Growth Des.*, 2020, **20**, 7588–7592.

10 O. Shemchuk, F. Grepioni and D. Braga, *Cryst. Growth Des.*, 2020, **20**, 7230–7237.

11 F. Liang, N. Wang, X. Liu, Z. Lin and Y. Wu, *Chem. Commun.*, 2019, **55**, 6257–6260.

12 Y. Li, X. Chen and K. M. Ok, *Chem. Commun.*, 2022, **3**, 3–6.

13 H. Wang, L. Liu, Z. Hu, J. Wang, M. Zhu, Y. Meng and J. Xu, *Inorg. Chem.*, 2023, **62**, 557–564.

14 Y. Deng, L. Wang, Y. Ge, L. Huang, D. Gao, J. Bi and G. Zou, *Chem. Commun.*, 2020, **56**, 9982–9985.

15 H. Tian, C. Lin, X. Zhao, S. Fang, H. Li, C. Wang, N. Ye and M. Luo, *Mater. Today Phys.*, 2022, **28**, 100849.

16 H. Wu, H. Yu, W. Zhang, J. Cantwell, K. R. Poeppelmeier, S. Pan and P. S. Halasyamani, *Cryst. Growth Des.*, 2017, **17**, 4405–4412.

17 Q. Wang, L. Wang, X. Zhao, L. Huang, D. Gao, J. Bi, X. Wang and G. Zou, *Inorg. Chem. Front.*, 2019, **6**, 3125–3132.

18 Z. Bai and K. M. Ok, *Inorg. Chem. Front.*, 2023, **10**, 1919–1925.

19 F. Zhang, X. Chen, M. Zhang, W. Jin, S. Han, Z. Yang and S. Pan, *Light: Sci. Appl.*, 2022, **11**, 7.

20 X. Chen, B. Zhang, F. Zhang, Y. Wang, M. Zhang, Z. Yang, K. R. Poeppelmeier and S. Pan, *J. Am. Chem. Soc.*, 2018, **140**, 16311–16319.

21 S. Niu, G. Joe, H. Zhao, Y. Zhou, T. Orvis, H. Huyan, J. Salman, K. Mahalingam, B. Urwin, J. Wu, Y. Liu, T. E. Tiwald, S. B. Cronin, B. M. Howe, M. Mecklenburg, R. Haiges, D. J. Singh, H. Wang, M. A. Kats and J. Ravichandran, *Nat. Photonics*, 2018, **12**, 392–396.

22 P. Li, C. Hu, Y. Li, J. Mao and F. Kong, *J. Am. Chem. Soc.*, 2024, **57**, 538–548.

23 W. Zeng, Y. Tian, X. Dong, L. Huang, H. Zeng, Z. Lin and G. Zou, *Chem. Mater.*, 2024, **36**, 2138–2146.

24 M. J. Dodge, *Appl. Opt.*, 1984, **23**, 1980.

25 G. Zhou, J. Xu, X. Chen, H. Zhong, S. Wang, K. Xu, P. Deng and F. Gan, *J. Cryst. Growth*, 1998, **191**, 517–519.

26 G. Ghosh, *Opt. Commun.*, 1999, **163**, 95–102.

27 J. R. DeVore, *J. Opt. Soc. Am.*, 1951, **41**, 416.

28 D. E. Zelmon, D. L. Small and D. Jundt, *J. Opt. Soc. Am. B*, 1997, **14**, 3319.

29 A. Tudi, S. Han, Z. Yang and S. Pan, *Coord. Chem. Rev.*, 2022, **459**, 214380.

30 J. Guo, A. Tudi, S. Han, Z. Yang and S. Pan, *Angew. Chem., Int. Ed.*, 2021, **60**, 3540–3544.

31 Q. Chen, C. Hu, M. Zhang and J. Mao, *Chem. Sci.*, 2023, **14**, 14302–14307.

32 Y. Yang, Y. Xiao, B. Li, Y. Chen, P. Guo, B. Zhang and X. Zhang, *J. Am. Chem. Soc.*, 2023, **145**, 22577–22583.

33 Y. Liu, X. Liu, S. Liu, Q. Ding, Y. Li, L. Li, S. Zhao, Z. Lin, J. Luo and M. Hong, *Angew. Chem., Int. Ed.*, 2020, **59**, 7793–7796.

34 M. Liang, Y. Zhang, E. Izvarin, M. J. Waters, J. M. Rondinelli and P. S. Halasyamani, *Chem. Mater.*, 2024, **36**, 2113–2123.

35 S. Jiang, J. Zhou, H. Wu, H. Yu, Z. Hu, J. Wang and Y. Wu, *Chem. Commun.*, 2020, **56**, 7104–7107.

36 X. Wang, M. Xia and R. Li, *Opt. Mater. (Amsterdam, Neth.)*, 2014, **38**, 6–9.

37 X. Chen, F. Zhang, Y. Shi, Y. Sun, Z. Yang and S. Pan, *Dalton Trans.*, 2018, **47**, 750–757.

38 X. Liu, L. Kang, P. Gong and Z. Lin, *Angew. Chem., Int. Ed.*, 2021, **60**, 13574–13578.

39 Z. Hu, L. Liu, R. Zhang, Q. Jing, H. Wang, J. Tian, J. Xu and P. S. Halasyamani, *J. Mater. Chem. C*, 2023, **1**, 3777.

40 H. Sha, B. Li, Z. Xiong, Z. Wang, C. Liu, R. Su, C. He, X. Yang and X. Long, *J. Mater. Chem. C*, 2021, **9**, 15886–15890.

41 W. Xiong, L. Chen, L. Huang, F. Guo, Y. Zhou and H. Yuan, *Cryst. Res. Technol.*, 2015, **50**, 250–254.

42 R. Li, *Z. Kristallogr.*, 2013, **288**, 526–531.

43 H. Fan, N. Ye and M. Luo, *Acc. Chem. Res.*, 2023, **56**, 3099–3109.

44 Y. Shen, Y. Zhou, X. Xue, H. Yu, S. Zhao and J. Luo, *Inorg. Chem. Front.*, 2022, **21**, 27.

45 D. Dou, Q. Shi, Y. Bai, C. Chen, B. Zhang and Y. Wang, *Mater. Chem. Front.*, 2023, **7**, 5924–5931.

46 J. Lu, Y. Lian, L. Xiong, Q. Wu, M. Zhao, K. Shi, L. Chen and L. Wu, *J. Am. Chem. Soc.*, 2019, **141**, 16151–16159.

47 X. Liu, P. Gong and Z. Lin, *Inorg. Chem.*, 2021, **60**, 10890–10894.

48 J. Lu, X. Liu, M. Zhao, X. Deng, K. Shi, Q. Wu, L. Chen and L. Wu, *J. Am. Chem. Soc.*, 2021, **143**, 3647–3654.

49 Z. Zhang, X. Liu, X. Liu, Z. Lu, X. Sui, B. Zhen, Z. Lin, L. Chen and L. Wu, *Chem. Mater.*, 2022, **34**, 1976–1984.

50 X. Liu, P. Gong and Z. Lin, *Inorg. Chem.*, 2021, **60**, 10890–10894.

51 *SAINT, version 7.60A*, Bruker Analytical X-Ray Instruments Inc., Madison, WI, 2008.

52 O. V. Dolomanov, L. J. Bourhis, R. J. Gildea, J. A. K. Howard and H. Puschmann, *J. Appl. Crystallogr.*, 2009, **42**, 339–341.

53 A. L. Spek, *J. Appl. Crystallogr.*, 2003, **36**, 7–13.

54 M. J. Frisch, *et al.*, *Gaussian 09*, Revision D.01, Gaussian, Inc, Wallingford CT, 2009.

55 T. Lu and F. Chen, *J. Comput. Chem.*, 2012, **33**, 580–592.

56 T. D. Kühne, M. Iannuzzi, M. Del Ben, V. V. Rybkin, P. Seewald, F. Stein, T. Laino, R. Z. Khaliullin, O. Schütt, F. Schiffmann, D. Golze, J. Wilhelm, S. Chulkov, M. H. Bani-Hashemian, V. Weber, U. Borštnik, M. Taillefumier, A. S. Jakobovits, A. Lazzaro, H. Pabst, T. Müller, R. Schade, M. Guidon, S. Andermatt, N. Holmberg, G. K. Schenter, A. Hehn, A. Bussy, F. Belleflamme, G. Tabacchi, A. Glöß, M. Lass, I. Bethune, C. J. Mundy, C. Plessl, M. Watkins, J. VandeVondele, M. Krack and J. Hutter, *J. Chem. Phys.*, 2020, **152**, 194103.

57 S. J. Clark, M. D. Segall, C. J. Pickard, P. J. Hasnip, M. I. J. Probert, K. Refson and M. C. Payne, *Z. Kristallogr.– Cryst. Mater.*, 2005, **220**, 567–570.

58 W. Wang, H. Fan and Y. Ye, *Polymer (Guildf).*, 2010, **51**, 3575–3581.

59 J. P. Perdew, K. Burke and M. Ernzerhof, *Phys. Rev. Lett.*, 1996, **77**, 3865–3868.

60 K. Liu, H. Fan, P. Ren and C. Yang, *J. Alloys Compd.*, 2011, **509**, 1901–1905.

61 J. Lin, A. Qteish, M. C. Payne and V. Heine, *Phys. Rev. B: Condens. Matter Mater. Phys.*, 1993, **47**, 4174.

62 M. Mutailipu, X. Su, M. Zhang, Z. Yang and S. Pan, *Inorg. Chem. Front.*, 2017, **4**, 281–288.

63 R. A. Nyquist and R. O. Kagel, *Infrared Spectra of Inorganic Compounds*, Elsevier, 1971.

64 X. Pan, H. Wu, S. Cheng and Z. Wang, *Inorg. Chem. Front.*, 2019, **7**, 101–107.

65 H. Luo, T. Tkaczyk, R. Sampson and E. L. Dereniak, *Semiconductor Photodetectors III*, 2006, vol. 6119, 61190J.

66 X. Hao, M. Luo, C. Lin, G. Peng, T. Yan, D. Lin, L. Cao, X. Long, G. Yang and N. Ye, *Inorg. Chem.*, 2020, **59**, 10361–10367.

67 J. Wang, X. Zhang, F. Liang, Z. Hu and Y. Wu, *Cryst. Growth Des.*, 2021, **21**, 7194–7200.

68 J. Wang, X. Zhang, F. Liang, Z. Hu and Y. Wu, *Dalton Trans.*, 2021, **50**, 11555–11561.

69 Y. Li, J. Lee and K. M. Ok, *Bull. Korean Chem. Soc.*, 2023, 1–6.

70 Y. Shen, L. Ma, G. Dong, H. Yu and J. Luo, *Inorg. Chem. Front.*, 2023, **22**, 12–14.

71 Y. Shen, Y. Zhou, X. Xue, H. Yu, S. Zhao and J. Luo, *Inorg. Chem. Front.*, 2022, **9**, 5226–5230.

72 L. Qi, X. Jiang, K. Duanmu, C. Wu, Z. Lin, Z. Huang, M. G. Humphrey and C. Zhang, *J. Am. Chem. Soc.*, 2024, **146**, 9975–9983.